Magnetic anisotropy due to localized structural defects in strained yttrium iron garnet thin films

Xingzhi Wang,[1] Jinho Lim,[1] Yi Li,[2] Hsu-Chih Ni,[1] Jonathan Schimmels,[1] Zhixin Zhang,[1] Jiangchao Qian,[1] Robert Busch,[1] Youfu Qian,[1,2] Phuoc Cao Van,[3] Jong-Ryul Jeong,[3] Axel Hoffmann,[1,*] and Jian-Min Zuo[1,4,†]

[1]*Materials Research Laboratory and Department of Materials Science and Engineering, The Grainger College of Engineering, University of Illinois Urbana-Champaign, Urbana, Illinois 61801, USA*

[2]*Materials Science Division, Argonne National Laboratory, Argonne, Illinois 60439, USA*

[3]*Department of Materials Science and Engineering, Chungnam National University, Daejeon 34134, Republic of Korea*

[4]*Monash Centre for Electron Microscopy, Monash University, 10 Innovation Walk, Clayton VIC, Australia*

(Received 4 December 2025; revised 23 June 2026; accepted 25 June 2026; published 11 August 2026)

Yttrium iron garnet (YIG, $Y_3Fe_5O_{12}$) thin films are promising material systems for quantum magnonics due to their ultralow magnetic damping and the capability of building on-chip spin wave devices to be coupled with superconducting microwave circuits. However, the default substrate for epitaxial YIG thin-film growth, $Gd_3Ga_5O_{12}$ (GGG), suffers from strong microwave absorption at cryogenic temperature due to the magnetic moment induced by the rare-earth element Gd. In this work, we study strained epitaxial YIG thin films grown on $Y_3Sc_2Ga_3O_{12}$ (YSGG), a rare-earth-free substrate compatible with cryogenic applications. Using cross-sectional scanning transmission electron microscopy along with strain mapping, we show the existence of spot-shape domain defects in the epitaxial YIG films and their connection with strain and stoichiometry, leading to drastically different magnetic properties such as perpendicular magnetic anisotropy, magnetic hysteresis loop, and magnetic damping. Applying high-resolution orientation mapping, we identify localized lattice rotations as the structural origins of these domains. We hypothesize that these domains are formed by a self-composed off-stoichiometry during the growth of the YIG thin films, as a mechanism to accommodate the relatively large lattice mismatch between YIG and YSGG. By elucidating the structure-property relationship in YIG/YSGG thin films, this work highlights a strain accommodation mechanism in complex oxides and provides guidance for future works on the applications of strained YIG thin films in quantum information.

DOI: 10.1103/d3lt-swsx

I. INTRODUCTION

Yttrium iron garnet is widely used in magnonics and spintronics due to its ultralow magnetic damping [1–9]. Recently, the rapid development of hybrid magnonics shows promise for magnons in quantum information science [10–13], with demonstration of magnon-qubit entanglement [14], magnon quantum sensing [15,16], and magnon quantum tomography [17]. However, to explore the potential of magnons towards quantum information applications in terms of propagating magnons, such as utilizing magnon nonreciprocity [18] and implementing on-chip microwave-to-optic quantum transduction [19], one needs to integrate YIG thin-film systems with cryogenic superconducting quantum circuits.

YIG thin films have most commonly been grown epitaxially on $Gd_3Ga_5O_{12}$ (GGG) substrates, thanks to GGG's near-perfect lattice matching with YIG. However, at milli-Kelvin temperature required for practical quantum information applications, Gd in GGG generates complex spin state [20,21], leading to considerable enhancement of microwave absorption and thus incompatibility with cryogenic microwave quantum circuits. To address this challenge, $Y_3Sc_2Ga_3O_{12}$ (YSGG), which contains no rare-earth elements, has been investigated as an alternative substrate for YIG thin films. Previous study has demonstrated that ultralow damping and strong on-chip magnon-photon coupling can be achieved in YIG/YSGG thin films down to as low as 2 K, a temperature at which YIG/GGG thin films suffer from significant enhancement of damping [22]. These encouraging results have led to a significant rise of research attention on epitaxial YIG/YSGG thin films for quantum magnonics in recent years [4,13,22–26].

An intrinsic challenge for epitaxial YIG/YSGG thin films is that compared to GGG ($a = 12.377$ Å), YSGG ($a = 12.426$ Å) has a significantly larger lattice mismatch with YIG ($a = 12.376$ Å), theoretically leading to a 0.4% tensile strain in a stoichiometric YIG thin film. To achieve strong magnonic coupling in hybrid devices, a sufficiently thick YIG film (on the order of 100 nm) is often required [22]. Established theoretical models of critical thickness of epitaxial thin films [27,28] and experimental evidence [25,29] show that at such thickness, YIG/YSGG thin films would be prone to strain relaxation by misfit dislocations, detrimental to their magnetic properties. In current literature, strain relaxation in epitaxial YIG/YSGG thin films remain under-explored, and most existing literature reports YIG/YSGG thin films with thickness considerably lower than 100 nm [4,13,22–26,30]. More importantly, there is also a lack of thorough structural analyses to confirm whether these films remain coherently strained or relaxed, and to clarify how any structural imperfections

*Contact author: axelh@illinois.edu
†Contact author: jianzuo@illinois.edu

correlate with their magnetic properties. Such insights would be invaluable for understanding structure-property relationships in YIG/YSGG systems and for guiding the development of high-quality YIG/YSGG thin films for quantum magnonics.

In this work, we report the structural characterization of thick YIG/YSGG thin films under different growth conditions serving as a structure control parameter, using scanning transmission electron microscopy (STEM) and scanning electron nanodiffraction (SEND) or 4D-STEM. Although all the films show good epitaxy to the YSGG substrates without obvious lattice dislocations under STEM, they show a large difference in the formation of inhomogeneous domains inside the films, which is reflected by the dark circular areas with different contrast in the transmission electron microscopy (TEM) images. Applying SEND strain and orientation mapping, we demonstrate that these domains are formed due to local lattice rotation and distortions, which suggests local variation in elemental composition. Self-composed off-stoichiometry has been reported as a common pathway for epitaxial oxide thin films to handle large lattice mismatches [31,32]. However, on the microscopic level, such off-stoichiometry is typically accommodated by the formation of planar defects, or amorphous regions [33–36]. The formation of the nanoscale domains observed in this work represents a different pathway for epitaxial thin films to handle off-stoichiometry and large lattice mismatch between film and substrate. The occurrence of these domains correlates to higher magnetic damping and anisotropy measured at cryogenic temperatures, with results showing a strong correlation between film uniformity and low-temperature magnetic resonance. These results provide guidance to future works on optimizing YIG/YSGG thin films for quantum magnonics.

II. METHODS

To study the correlation between structural defects and magnetic properties, we prepared three epitaxial YIG thin films deposited on YSGG substrates under different growth conditions. For the first sample, denoted YIG/YSGG-1, the YIG film was sputter deposited at Chungnam National University using a laboratory-customized YIG target with an optimized Y:Fe ratio [37,38]. The other two samples, denoted YIG/YSGG-2 and YIG/YSGG-3, were deposited at Argonne National Laboratory using a commercial sintered oxide mixture $Y_3Fe_5O_{12}$ target [9,39], with substrate-target distances of 50 mm (YIG/YSGG-2) and 80 mm (YIG/YSGG-3), respectively. All the three as-deposited YIG/YSGG films were initially amorphous and were subsequently annealed in air at 850 °C for 3 h and slowly cooled down to room temperature at a rate of 30 °C/h in order to establish the epitaxial texture along the YSGG substrate. Because the as-deposited YIG films are amorphous, variations in substrate-target distance and Ar pressure primarily affect the Y:Fe stoichiometry by modifying the sputtering plasma profiles of Y and Fe species.

To study the magnetic properties of the three samples, we conducted ferromagnetic resonance (FMR) at both room temperature and cryogenic temperature, in order to characterize the magnetic damping and strain-induced magnetic anisotropy. The room-temperature FMR was performed by fixing the frequency and sweeping the magnetic field using the field-modulation technique, while the cryogenic FMR was performed by fixing the field and sweeping the frequency using a vector network analyzer (VNA). We also conducted superconducting quantum interference device (SQUID) measurements for the magnetic moments and the magnetic hysteresis loops.

To visualize the nanoscopic structures of the thin films, electron-transparent cross-sectional samples were prepared using an FEI Helios 600i or FEI Scios 2 focused ion beam (FIB). The nonconductive YIG thin films were sputter coated with a Pd/Au layer by an Emscope SC 500 sputter coater before FIB experiments. To protect the top surfaces of YIG thin films from ion-beam damage, layers of Pt were coated *in situ* by first the electron beam, then the ion beam. The lamellar cut out by FIB were lifted out and thinned by ion beam until they showed transparency under electron beam at 5 keV. The samples were then imaged using TEM, STEM, and SEND. All data were acquired using a standard double-tilt holder, aligning the $[11\bar{2}]$ zone axis of YIG with the electron beam. Dark-field (DF) TEM images were recorded using a JEOL 2010 TEM with a Gatan Orius SC1000 CCD detector with a few seconds exposure time. Atomic-resolution STEM images were recorded using a ThermoFisher Themis Z S/TEM with a high-angle annular dark-field (HAADF) detector with collection angles from 51 to 200 mrad. The beam current was ∼100 pA, with a beam convergence angle of 18 mrad. The dwell time was 2 μs and the scan area was 2048×2048 pixels. SEND data were collected using a ThermoFisher Talos F200X G2 S/TEM with a Ceta 16M detector. Diffraction patterns were typically collected with the size of 512×512 pixels, scanned over an area 128×128 pixels (1μm × 1μm), with a dwell time of 30 ms and beam convergence angle of 0.6 mrad. Energy-dispersive x-ray spectroscopy (EDS) was performed using a ThermoFisher Talos F200X G2 S/TEM with a Super-X SDD EDS detector with four segments and a fixed sample position. Only detector segments reading strong signals were used for data collection. The sample was tilted by ∼2° to an off-zone-axis orientation to avoid channeling effects. The beam current was ∼0.8 nA, with a beam convergence angle of 10.5 mrad. The scanning area was 384×384 pixels (148×148 nm^2), with a dwell time of 5 μs. Spectra were collected from 0 to 20 keV, with a 20-eV energy resolution. The scanning was performed continuously until the signal of the $K\alpha$ edge of Fe reached 5000–10 000 counts, typically in 30–40 min. To ensure the accuracy of quantitative EDS measurements, we performed EDS measurements following the same procedures on a single-crystalline YIG as a standard calibration sample. The quantified Y/Fe ratio in this standard sample was 0.59 ± 0.04, closely agreeing with the expected stoichiometry of $Y_3Fe_5O_{12}$.

We followed literature reports for the quantitative analysis of the collected data. The details of the analysis are listed in Supplemental Material [52].

III. RESULTS

Figure 1 compares the SQUID and FMR line shapes of the three YIG samples. From the SQUID data, the three samples show similar magnetizations (M_s), with

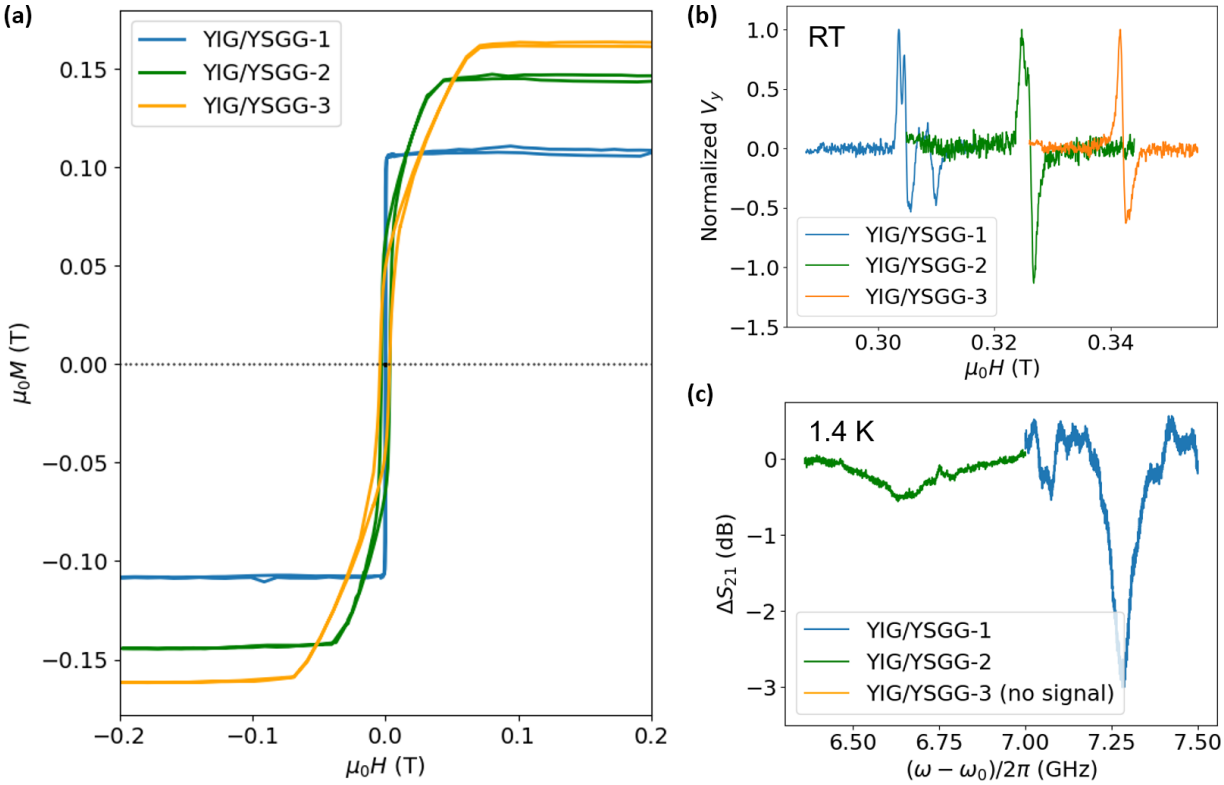

FIG. 1. (a) Magnetic hysteresis loops of the three YIG/YSGG thin films measured by a superconducting quantum interference device (SQUID). (b) Ferromagnetic resonance (FMR) signal of three YIG/YSGG thin films at 10.0 GHz. (c) Vector network analyzer (VNA) measurements of the magnetic resonance of the three thin films at 1.4 K. YIG/YSGG-3 shows no resonance and is therefore not shown in the figure.

YIG/YSGG-1 exhibiting a smaller value. However, the FMR line shapes show clear difference in resonance field, showing a large variation in the effective magnetization M_{eff} [Fig. 1(a)]. The extracted M_{eff} from the in-plane Kittel equation, $\omega = \gamma\mu_0\sqrt{H(H + M_{\text{eff}})}$, are summarized together with measured M_s in Table I. The main feature is that M_{eff} and M_s are comparable for YIG/YSGG-1 but show large discrepancy for YIG/YSGG-2 and YIG/YSGG-3. This suggests a strong perpendicular magnetic anisotropy at the YIG/YSGG interface due to lattice mismatch, which is typically caused by the interfacial strain due to lattice mismatch.

Next, we focus on the FMR linewidths of the three samples. At room temperature, the three YIG films show similar total linewidth broadening [Fig. 1(b)]. This is dominated by the multi-peak features as a consequence of heterogeneous formation during the annealing process, and is quite common in epitaxial YIG films. However, at cryogenic temperature down to 1.4 K, the YIG/YSGG-1 sample still shows a reasonable absorption peak but the YIG/YSGG-2 shows a much broader peak as compared with YIG/YSGG-1. The YIG/YSGG-3 sample, which shows the lowest M_{eff} in Table I, does not show any cryogenic FMR signal even after background subtraction [Fig. 1(c)]. These results suggest that the YIG/YSGG-1 sample, which shows the best $M_{\text{eff}} - M_s$ agreement and the best cryogenic FMR linewidth, should have the best crystallinity, and YIG/YSGG-2 and YIG/YSGG-3 are expected to have higher lattice mismatch, and possibly lower crystallinity.

TABLE I. Effective magnetization (M_{eff}) and saturation magnetization (M_s) of the three YIG/YSGG thin films measured by FMR and SQUID. Uncertainties were estimated as 95% confidence intervals of the fits.

Film	$\mu_0 M_{\text{eff}}$ (T)	$\mu_0 M_s$ (T)
YIG/YSGG-1	0.123 ± 0.005	0.111 ± 0.003
YIG/YSGG-2	0.072 ± 0.005	0.147 ± 0.004
YIG/YSGG-3	0.038 ± 0.005	0.163 ± 0.005

To confirm the speculated differences in lattice mismatch as suggested by the SQUID and FMR data, we conducted high-resolution x-ray diffraction (XRD) for the three samples. As shown in Fig. 2(a), all three YIG films show clear YIG 444 XRD peaks at $2\theta \sim 51.5°$, which appear on the right side of the YSGG peak at $2\theta \sim 50.8°$. The presence of Laue oscillations in the XRD of all three thin films shows that the films are smooth. From the XRD data, we find that the YIG/YSGG-1 sample shows a significantly smaller difference between the YIG and YSGG diffraction peaks as compared with YIG/YSGG-2 and YIG/YSGG-3 samples, confirming a smaller lattice mismatch for YIG/YSGG-1 and verifying the speculation from the SQUID and FMR measurements. X-ray reciprocal-space mapping (RSM) further confirms that the lattices of the film and the substrate are well matched in the in-plane direction, suggesting that the films are fully strained without relaxations [Figs. 2(b)–2(d)]. However, we also note that the lattice mismatch in different thin films only varies

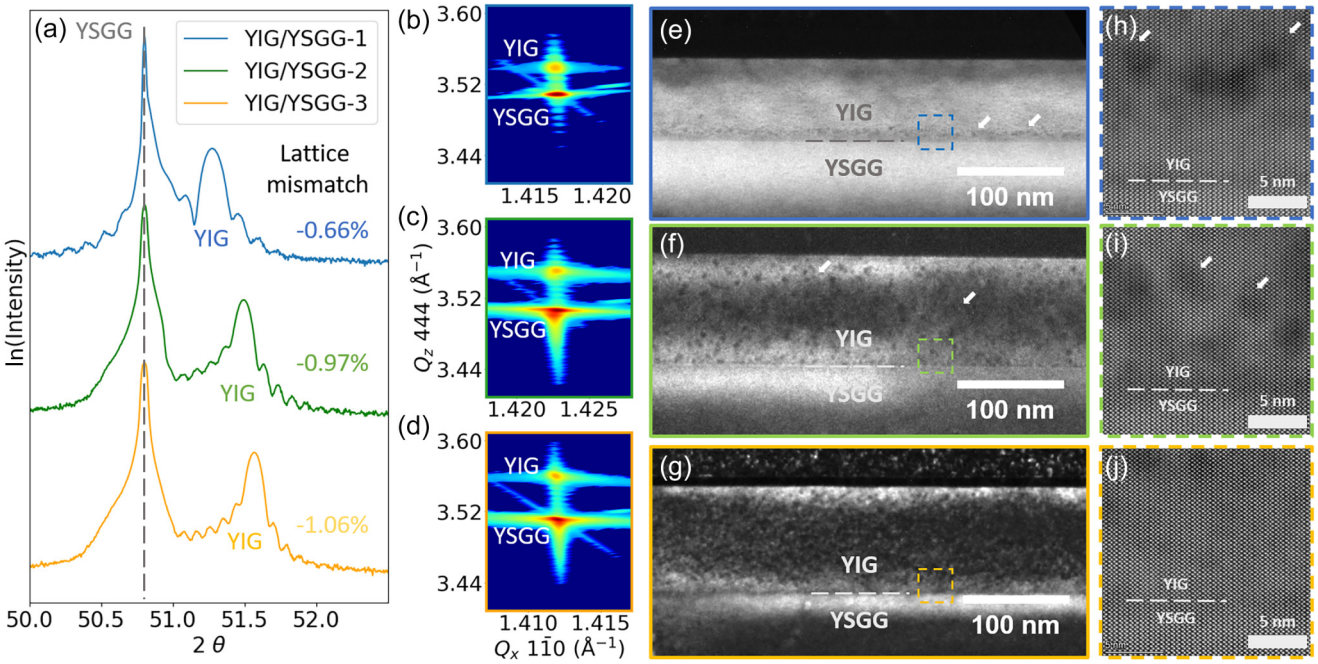

FIG. 2. (a) High-resolution XRD of the three YIG/YSGG thin films. Dotted line marks the position of diffraction peaks corresponding to the (444) reflection of YSGG. Lattice mismatches were calculated from the distance between the two diffraction peaks, using the YSGG peaks as references. (b)–(d) Asymmetric x-ray reciprocal-space mappings of (a) YIG/YSGG-1, (b) YIG/YSGG-2, and (c) YIG/YSGG-3 near the (642) Bragg diffraction peak. (e)–(g) Dark-field TEM images of the thin films formed using the 222 diffracted beam under an approximate two-beam condition. Dashed lines mark the interface between YIG and YSGG. Dark-field images with other diffracted beams are shown in Fig. S2 of the Supplemental Material [52]. The white arrows point to instances of spot-shaped domains inside the thin films. (h)–(j) Atomic resolution STEM HAADF image of thin films in (b)–(d) at the YIG/YSGG interface. Images are taken on the [11$\bar{2}$] zone axis.

within a small range of ∼0.4%. This observation indicates that lattice strain might not be the only factor leading to the large magnetic anisotropy observed in these YIG/YSGG thin films.

To elucidate the structural origins of the observed magnetic anisotropy in YIG/YSGG thin films studied here, detailed characterization of the structures of these films at nanoscale is required. To achieve this goal, we applied focused ion beam (FIB) to obtain cross-sectional samples of the YIG thin films. These samples are then characterized by electron microscopy. The thickness of the films are measured from cross-sectional TEM [Figs. 2(e)–2(g)]. YIG/YSGG-1 has a thickness of 80 nm, while YIG/YSGG-2 and YIG/YSGG-3 have a thickness of 100 nm. We applied dark-field (DF) TEM to further confirm the absence of lattice dislocations in the YIG/YSGG thin films. No dark or bright contrasts corresponding to lattice dislocations are observed in DF TEM images formed with electron beams diffracted by different lattice planes for any of the three thin films, suggesting that no significant lattice dislocations exist in these films [Figs. 2(e)–2(g) and S2 of the Supplemental Material [52]]. Remarkably, even YIG/YSGG-3, with an over 1% lattice mismatch with the substrate, remains defect-free in our observation. Atomic resolution STEM high angle annular dark field (HAADF) at the interfaces between YIG and YSGG in the three thin films also confirms that the lattices are coherent across the interface, with no sign of mismatch of defects [Figs. 2(h)–2(j)]. These results confirm that the thin films remain fully strained without relaxation or dislocations at their relatively high thicknesses.

Although the thin films appear fully strained, from both the TEM and the STEM images, it can be seen that there exists spot-shaped contrasts inside the thin films. In YIG/YSGG-1, these contrasts are small and distribute primarily along the interface [Fig. 2(e)], while in YIG/YSGG-2 and YIG/YSGG-3, these contrasts are larger and distribute across the entirety of the film [Figs. 2(f) and 2(g)] [5,40]. It should be noted that these contrasts do not appear to be the same phenomenon as domains of lattice defects shown in the work of Costa *et al.* [40]. As shown in atomic resolution STEM-HAADF, the lattice is clear and coherent both inside and outside of the regions of the contrasts [Figs. 2(h)–2(j)]. In $2\theta - \omega$ XRD scans of the films, no additional peak besides the 444 film normal Bragg diffraction peak is visible, confirming that the inhomogeneous contrasts observed by TEM are not caused by the formation of new crystalline phases [Fig. S3(a) of the Supplemental Material [52]]. A correlation is observed in the full width at half maximum of the XRD rocking curves of the YIG/YSGG films near the Bragg peak of YIG, and the relative density of the spot-shaped contrasts in the films, indicating that the contrasts are correlated to the crystal structures of the thin films [Figs. S3(b) and S3(c) of the Supplemental Material [52]]. Further, YIG/YSGG-1, with the lowest magnetic anisotropy, shows the lowest density of spot-shaped domains, while YIG/YSGG-3, with the highest magnetic anisotropy, shows the highest density of spot-shaped domains. As such, it is likely that these spot-shaped domains contribute to the magnetic anisotropy of the YIG/YSGG thin films. Hence, more detailed understanding is needed to un-

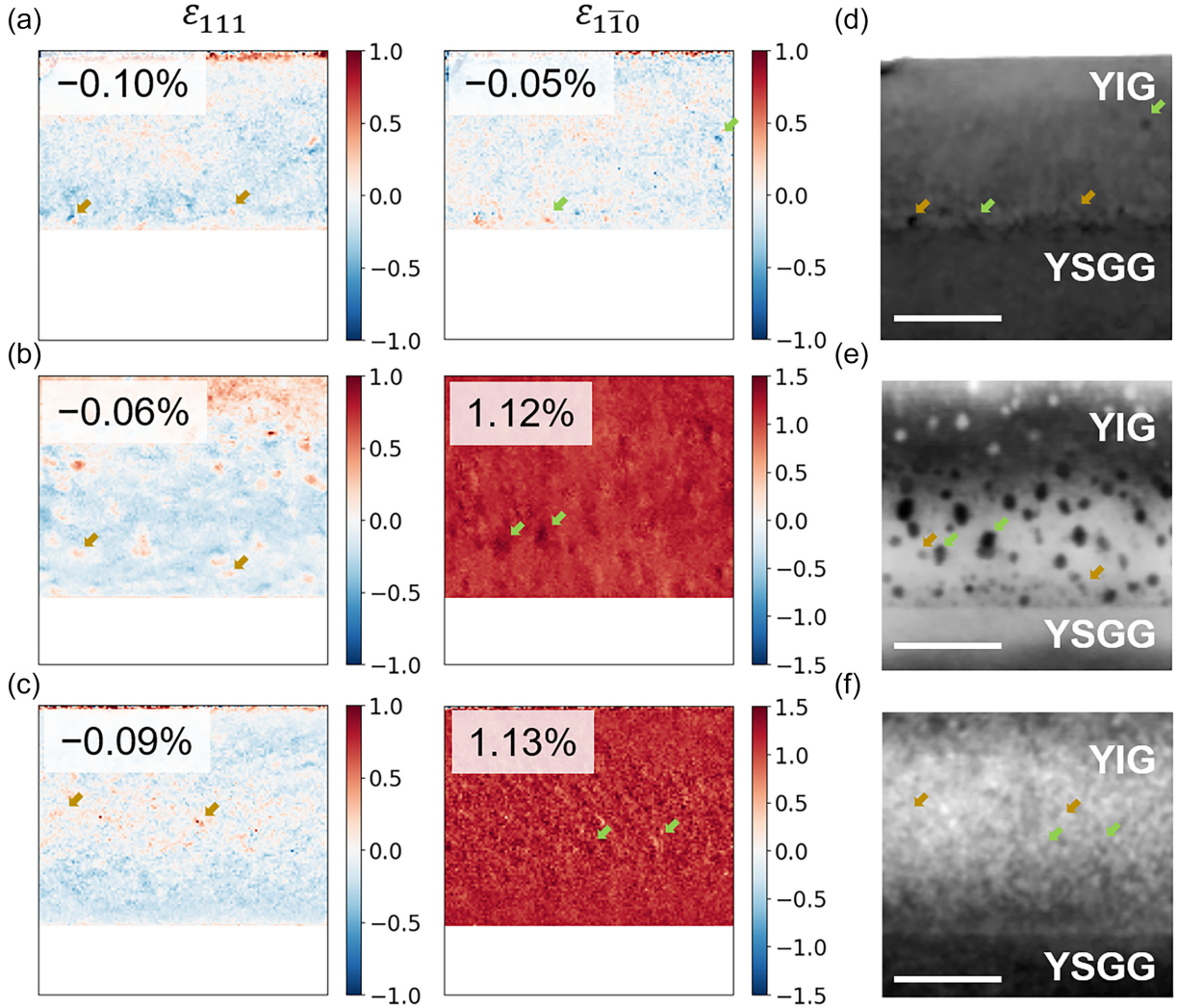

FIG. 3. Maps of strain tensors $\varepsilon_{1\bar{1}0}$ and ε_{111} in the YIG film from SEND of (a) YIG/YSGG-1, (b) YIG/YSGG-2, and (c) YIG/YSGG-3. ε_{111} is defined as the strain along the out-of-plane [444] direction, and $\varepsilon_{1\bar{1}0}$ is defined as the strain along the in-plane [1$\bar{1}$0] direction. The inset numbers represent the average strain inside the film. Strain is defined by $(a - a_0)/a_0$, where a is the lattice constant measured from SEND data; a_0 is the unstrained lattice constant of YIG calculated using elastic constant reported in literature [24] (more details in Supplementary Methods, Sec. II, of the Supplemental Material [52]). Arrows indicate examples of regions with localized strains. (d)–(f) Virtual bright-field images constructed from the SEND data constructed from the SEND datasets of the three thin films. (d) YIG/YSGG-1, (e) YIG/YSGG-2, and (f) YIG/YSGG-3. Arrows represent the spotlike domains corresponding to the regions with localized strains shown in (a)–(c). Scale bars represent 50 nm.

derstand their structural origin and their role in magnetic anisotropy.

SEND, with high resolution in both real and reciprocal space, is an ideal tool for understanding the underlying structural origins of these nanoscale domains. In SEND, a nanometer-sized electron probe is raster scanned across a two- dimensional field of view, with a direct electron detector recording the diffraction patterns at each scan location [41]. An abundance of structural information can be extracted from the resulting dataset of diffraction patterns, such as lattice strain [41,42] and lattice orientations [41,43], as detailed later. For the YIG/YSGG thin films, we choose to take diffraction on the [11$\bar{2}$] zone of YIG, as a major zone axis. Example electron-diffraction patterns of the YIG/YSGG-2 with indexing are shown in Fig. S4 of the Supplemental Material [52].

We calculated the strain maps of the three thin films using their SEND data (Fig. 3). Strain tensors were calculated from the diffraction patterns following a previously reported method based on circular Hough transform [42]. Figure 3 shows the 2D spatial maps of the strain tensors ε_{111} and $\varepsilon_{1\bar{1}0}$ of the three YIG/YSGG thin films. Here, strain ε is defined as $(a - a_0)/a_0$, where a is the lattice constant of YIG measured from diffraction patterns, and a_0 is the unstrained lattice constant of YIG. The value of a_0 is calculated for each sample based on the linear elastic theory, by $a_0 = a_{\text{sub}} - (1 - \mu_{111})/(1 + \mu_{111})\ (a_{\text{sub}} - a_{111})$ [24], where a_{111} is the out-of-plane lattice parameter of YIG measured from SEND data, μ_{111} is the Poisson coefficient for (111)-oriented YIG films reported in previous literature [24], and a_{sub} is the average lattice parameter of YSGG measured from SEND data (Fig. S5 of the Supplemental Material [52]). The results show

that in the in-plane direction, YIG has almost the same lattice constants as the YSGG substrate, while in the out-of-plane direction YIG is almost unstrained, with a slight compression in the lattice constants. This observation suggests that the thin films are under typical tensile strains, in good agreement with the x-ray RSM results [Figs. 2(b)–2(d)]. Notably, in all three thin films, the distribution of strains is not uniform. Rather, regions in which the strains deviate from their surroundings can be observed in all three thin films. The distribution of these localized strain regions roughly corresponds to the locations of the spot-shaped domains, as can be seen in the virtual bright-field images constructed from the SEND datasets [Figs. 3(d)–3(f) and Fig. S6 of the Supplemental Material [52]]. The observation of localized strains inside the spot domains suggests that local lattice distortions may be present inside these domains. To reveal the nature of the lattice distortions in the spotlike domains, we performed lattice orientation mapping on the SEND data of YIG/YSGG-2 based on the method reported by Yuan *et al*. (Fig. 4) [43]. This method predicts the orientations of lattices from electron-diffraction patterns using a neural network trained on simulated diffraction patterns at different lattice tilt angles [Fig. 4(a)]. Similar to the strain maps, in both in-plane [Fig. 4(b)] and out-of-plane [Fig. 4(c)] orientation maps, regions with localized lattice rotations can be observed. Such an observation suggests that the nature of the localized lattice distortions in the spotlike domains originates from rotations of the local lattices. To visualize this local lattice rotation more directly, we applied atomic resolution STEM imaging on YIG/YSGG-2 (Fig. 5). In the atomic resolution STEM-HAADF image [Fig. 5(a)], the positions of yttrium (Y) atoms, the heaviest atom in the YIG crystal, can be seen clearly. Taking a line HAADF intensity profile along one row of Y atoms in this direction shows a profile consisted of alternating twin peaks and singles peaks, corresponding to the positions of Y atoms in the garnet lattice [Fig. 5(b)]. Traversing from a spotlike domain to the background, the intensity profile in Fig. 5(b) shows that the twin peaks corresponding to the dumbbells of Y atoms are better resolved inside the spot-shaped domain (Left) than in the background (Right), which can be attributed to slight differences in lattice orientations in the two regions, as confirmed by simulated STEM-HAADF images of YIG with lattice tilt (Fig. S7 of the Supplemental Material [52]). Combined with the orientation mapping results, these observations confirm that the domains are indeed originated from localized lattice rotations.

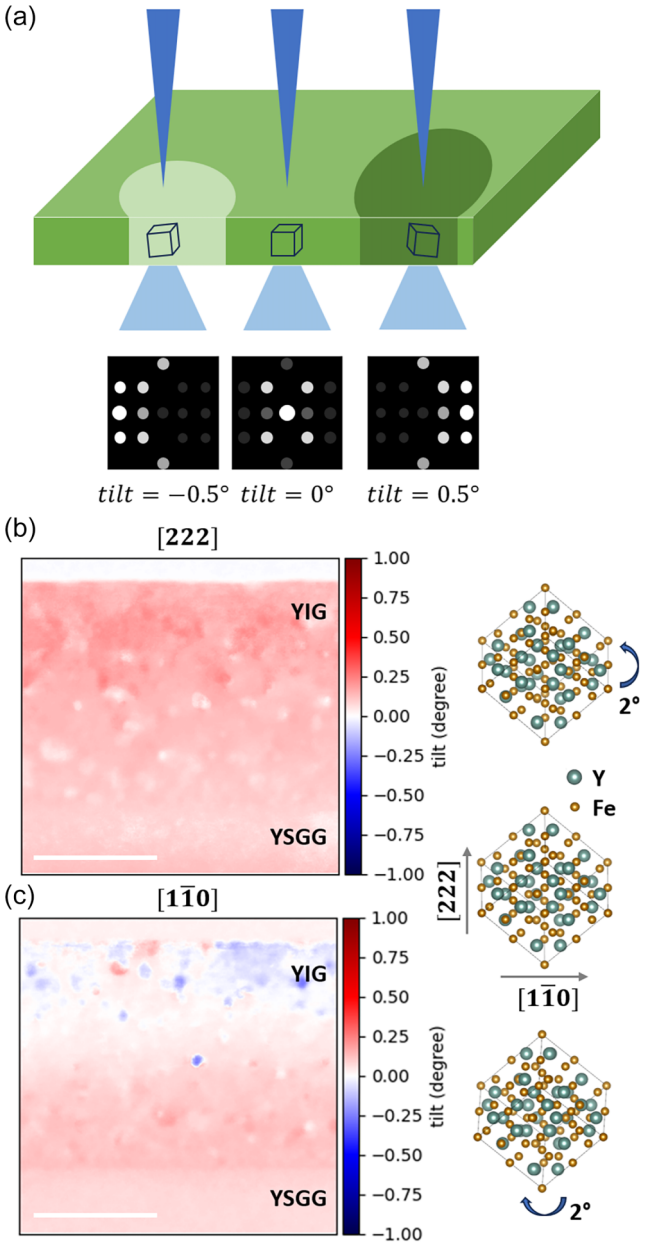

FIG. 4. (a) A schematic of lattice orientation mapping from SEND data. (b), (c) Orientation maps in (b) [222] (film normal) zone axis and (c) [1$\bar{1}$0] zone axis of YIG/YSGG-2. The atomic models provide a visualization of the in-plane and out-of-plane rotations of a YIG lattice. O atoms are omitted from the models for visual clarity. Crystallography data from the NIST Inorganic Crystal Structure Database (ICSD) No. 33931. Scale bars represent 50 nm.

IV. DISCUSSION

In this work, we did not attempt to identify the specific mechanisms by which different growth conditions lead to formation of structural defects; instead, we focus on correlating structural defects with the resulting magnetic properties of the YIG films. From the experimental results of SEND and atomic resolution STEM imaging, it can be concluded that the spot-shaped contrasts originated from localized lattice distortions and rotations inside the YIG thin film, thus making them nanosized domains. From Figs. 4(b) and 4(c), it can be seen that while the regions inside the domains show different lattice orientations compared to their surroundings, each of the spot-shaped domains also has a different lattice orientation. As such, the spotlike domains should not be seen as a new distinct crystalline phase that emerged from the YIG thin films, but should rather be more appropriately considered as intrinsically random structural inhomogeneities in an otherwise uniform thin film. The presence of these inhomogeneities reduces the effective mosaic block size of the matrix in the thin films for x-ray diffraction, as evidenced by the peak broadening in the XRD rocking curves [Fig. S3(b) of the Supplemental Material [52]]. This may explain the observed positive correlations between the density of spot-

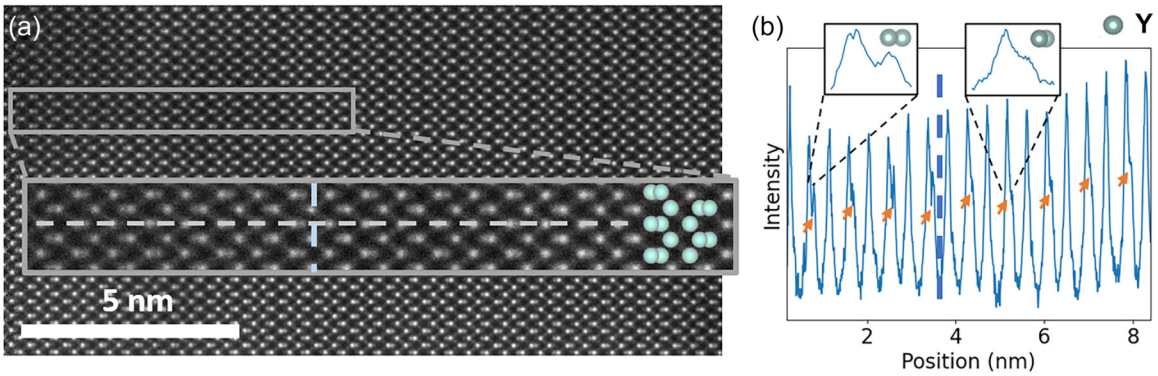

FIG. 5. (a) Atomic resolution STEM HAADF image of the YIG film in YIG/YSGG-2. Blue dotted line indicates the boundary between a spot-shaped region and background. Atomic model in the inset shows the expected positions of Y atoms in an YIG lattice. Crystallography data from ICSD No. 33931. (b) Integrated HAADF intensity along the gray dotted line in (a). x axis indicates the distance from the left end of the dotted line.

shaped domains and the magnetic anisotropy of the thin films. Magnetocrystalline anisotropy has been commonly observed in YIG thin films, where epitaxial strains reduce the symmetry of YIG lattice, leading to an increase in magnetic anisotropy [23,25,44–46]. However, in our thin films, we observed significantly higher levels of magnetic anisotropy at the same level of strains compared to previous literature [23,25,44–46]. This suggests that there exist additional factors in our YIG/YSGG thin films. In YIG, the ferrimagnetism of YIG originates from the nonzero net magnetic moments of Fe^{3+} in fixed lattice sites [47] [Fig. 6(a)]. Localized domains with different lattice orientations in the YIG thin film interrupt the alignment of spins in neighboring lattice, hence leading to increased magnetic anisotropy, as depicted in the schematic Fig. 6(c). A similar effect has previously been reported by Krysztofik *et al.* [48].

The question that remains to be answered is, what causes the formation of the spot-shaped domains with localized lattice rotations? Strain-induced lattice rotation is a well-understood phenomenon in epitaxial oxide thin films [49]. However, observations of such lattice rotations typically report rotations on the level of single unit cells with the distortion of metal–oxygen bonds [49]. The spot-shaped domains we observed far exceed the dimension of unit cells, and therefore cannot be simply explained as a strain-induced effect. From the in-plane strain of YIG ($\varepsilon_{1\bar{1}0}$, Fig. 3), unstrained lattice parameters of YIG (a_{YIG}) are calculated [24]. Figure 6(b) shows a histogram of the average values of a_{YIG} in different spot-shaped domains in YIG/YSGG-2, as well as the average a_{YIG} in the background, measured from SEND data [Figs. 3(b) and 3(e)]. It should be noted that these values are considerably smaller than the bulk lattice constant of YIG (12.376 Å). Such a shift in lattice parameters indicates substitutions of atoms in YIG lattices. In YIG, it has been known that both Y and Fe can substitute atoms of the other element by occupying the lattice sites of the substituted atoms, leading to an elemental composition that deviates from the nominal $Y_3Fe_5O_{12}$ stoichiometry [24]. Since Fe^{3+} has a smaller radius than Y^{3+}, substitution of Y by Fe will lead to a lattice contraction in YIG [24]. Elemental mapping by energy-dispersive x-ray spectroscopy (EDS) confirms the deficiency of Y in all three thin films, and YIG/YSGG-3, with the highest magnetic anisotropy, also shows the lowest Y-to-Fe ratio (Fig. S8 of the Supplemental Material [52]). In the lattice of YIG, Y atoms locate intermittently between Fe sites [Fig. 6(a)]. Therefore, replacing an Y^{3+} with a smaller Fe^{3+} can lead to contraction of its surrounding lattice sites, introducing a tilt into the lattice, similar to the observations made by Scarisoreanu *et al.* [50]. Such an effect accounts for the localized lattice orientation changes (Fig. 4) observed in this work. It is also of note that the values of a_{YIG} inside the spot-shaped domains are larger than the average a_{YIG} in the background, indicating that the spot-shaped domains have higher Y content than their surrounding regions.

As a typical ceramic material, YIG has a rigid ionic crystal lattice, and is expected to have low tolerance for lattice strain. We have, however, observed up to 1% strain in YIG/YSGG thin films, without any evidence of strain relaxation by lattice dislocations. Such an unusual resilience to strain may be explained by the change in lattice constant induced by changes in elemental compositions. Indeed, literature report has shown that in epitaxial thin films grown by pulsed laser deposition, the films can go through self-composed cation off-stoichiometry to accommodate the mismatch between the lattices of the film and the substrate, leading to significantly enhanced critical thicknesses [31,32]. Our observations reveal that such a similar process is likely occurring in the YIG/YSGG thin films. Unlike previous literature reports, in which off-stoichiometry occurred uniformly inside the thin film [31,32], the YIG/YSGG thin films form localized domains with off-stoichiometry. Our experimental observations indicate that the density of the spot-shaped domains inside the thin films is positively correlated to the strain in the films (Figs. 3 and S3 of the Supplemental Material [52]), further supporting that these domains help to accommodate epitaxial strains in the thin films and prevent them from going through misfit dislocation-related relaxations. These observations potentially suggest a pathway for the accommodation of strain induced by lattice mismatch in YIG thin films.

All three thin films studied in this work are YIG on YSGG substrates, fabricated by sputter deposition followed by annealing in two different laboratories, yet these films all show spot-shaped domains at drastically different densities. This observation suggests that conditions of sputter deposition,

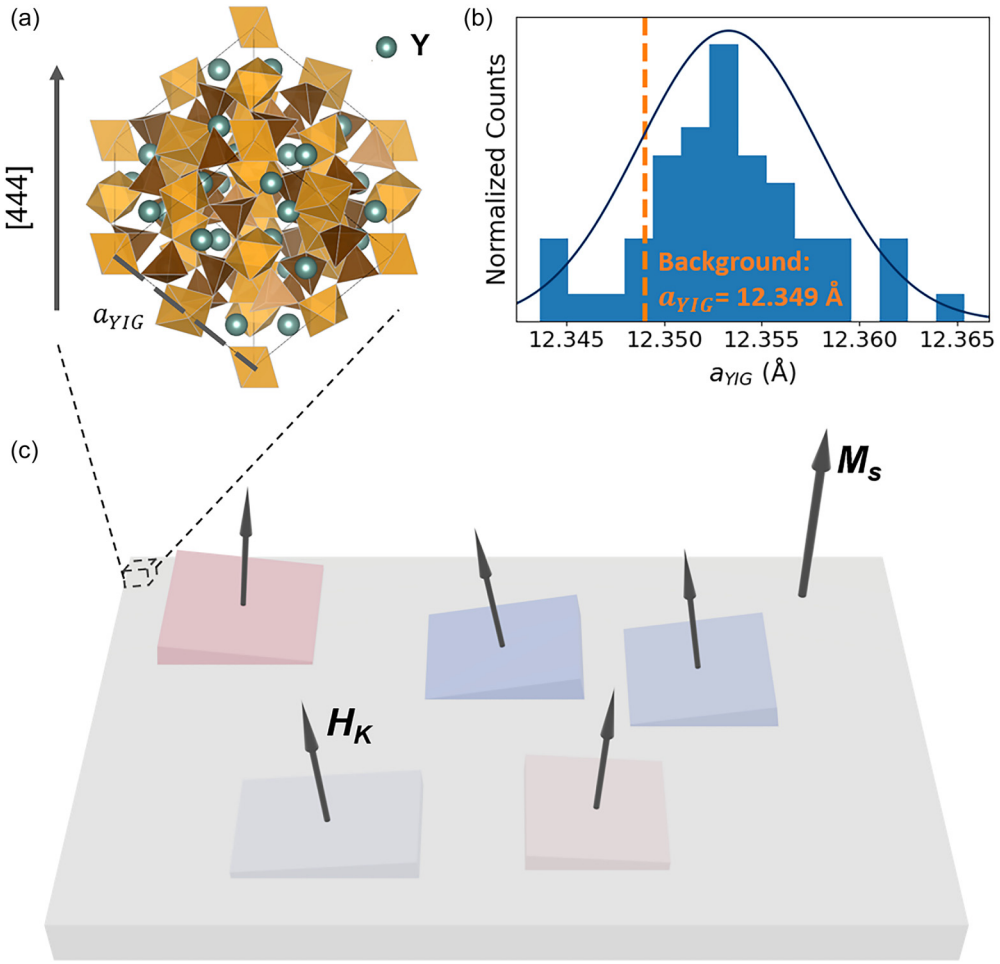

FIG. 6. (a) Atomic model of YIG showing the positioning of Y atoms between Fe sites (light brown: octahedral sites; dark brown: tetrahedral sites) in a unit cell. O atoms are omitted. Crystallography data from ICSD No. 33931. (b) Histogram of measured lattice constant, corrected for tetragonal distortion, of YIG (a_{YIG}) in different spot-shaped domains in YIG/YSGG-2. Dotted line marks the average a_{YIG} in the background region outside of the spot-shaped domains in YIG/YSGG-2. (c) A schematic showing a possible distribution of the magnetization directions of the spot-shaped domains and the bulk of the film.

such as the target, and the distance from the substrate to the target, have impacts on the defect densities of the resulting thin films, and hence their magnetic performance.

Another widely used technique for YIG thin-film growth is pulsed laser deposition (PLD), which is particularly effective at preserving the stoichiometry of complex oxide targets and enabling high-quality epitaxial growth. Although epitaxial YIG films have been successfully grown on YSGG substrates using PLD [51], it remains unclear whether the spot-shaped domains observed in sputter-anneal-grown films also form in PLD-grown films as a strain-relaxation mechanism. Addressing this question would provide valuable insight into the influence of growth kinetics on strain relaxation in YIG and help establish whether such domain structures are a universal feature of YIG/YSGG heterostructures or are specific to particular growth methods.

V. CONCLUSION

In this work, we examined three YIG/YSGG thin films prepared by sputter deposition. These thin films show significantly different magnetic anisotropy. While all three thin films are dislocation-free, we observed spot-shaped domains in the cross sections of all three films. The amounts and densities of the spot-shaped domains correlate to the magnetic anisotropy of the thin films. Strain and orientation mappings from SEND reveal that these domains correspond to localized variations of lattice constants and orientations. We hypothesize that these domains are formed as a result of Fe replacing Y in the lattice of YIG, leading to an Y-deficient film, indicating a pathway for expitaxial oxide thin films to handle large lattice mismatches. The localized lattice distortions and rotations induced by this process may explain the high magnetic anisotropy of these thin films. Future works on developing YIG/YSGG thin films for quantum magnonics should focus on achieving better controls over the elemental composition of the YIG/YSGG thin films [52].

ACKNOWLEDGMENTS

The experimental work, including sample preparation, TEM and XRD measurements, ferromagnetic resonance, and data analysis at UIUC, and YIG thin-film growth and SQUID measurements at Argonne, was primarily supported by the U.S. DOE, Office of Science, Basic Energy Sciences, Mate-

rials Sciences and Engineering Division under Contract No. DE-SC0022060. This work was carried out in part in the Materials Research Laboratory Central Research Facilities, University of Illinois, which is partially supported by NSF Award No. DMR-2309037.

DATA AVAILABILITY

The data that support the findings of this article are openly available on [54].

[1] A. A. Serga, A. V. Chumak, and B. Hillebrands, YIG magnonics, J. Phys. D: Appl. Phys. **43**, 264002 (2010).

[2] Y. Sun, H. Chang, M. Kabatek, Y.-Y. Song, Z. Wang, M. Jantz, W. Schneider, M. Wu, E. Montoya, B. Kardasz, B. Heinrich, S. G. E. te Velthuis, H. Schultheiss, and A. Hoffmann, Damping in yttrium iron garnet nanoscale films capped by platinum, Phys. Rev. Lett. **111**, 106601 (2013).

[3] M. B. Jungfleisch, W. Zhang, W. Jiang, H. Chang, J. Sklenar, S. M. Wu, J. E. Pearson, A. Bhattacharya, J. B. Ketterson, M. Wu, and A. Hoffmann, Spin waves in micro-structured yttrium iron garnet nanometer-thick films, J. Appl. Phys. **117**, 17D128 (2015).

[4] J. Gückelhorn, T. Wimmer, M. Müller, S. Geprägs, H. Huebl, R. Gross, and M. Althammer, Magnon transport in $Y_3Fe_5O_{12}$/Pt nanostructures with reduced effective magnetization, Phys. Rev. B **104**, L180410 (2021).

[5] J. Qian, Y. Li, Z. Jiang, R. Busch, H.-C. Ni, T.-H. Lo, A. Hoffmann, A. Schleife, and J.-M. Zuo, Unraveling the origin of antiferromagnetic coupling at YIG/permalloy interface, Phys. Rev. Mater. **8**, 104405 (2024).

[6] H. Yu, O. D'Allivy Kelly, V. Cros, R. Bernard, P. Bortolotti, A. Anane, F. Brandl, R. Huber, I. Stasinopoulos, and D. Grundler, Magnetic thin-film insulator with ultra-low spin wave damping for coherent nanomagnonics, Sci. Rep. **4**, 6848 (2014).

[7] M. Collet, O. Gladii, M. Evelt, V. Bessonov, L. Soumah, P. Bortolotti, S. O. Demokritov, Y. Henry, V. Cros, M. Bailleul, V. E. Demidov, and A. Anane, Spin-wave propagation in ultra-thin YIG based waveguides, Appl. Phys. Lett. **110**, 092408 (2017).

[8] C. Hauser, T. Richter, N. Homonnay, C. Eisenschmidt, M. Qaid, H. Deniz, D. Hesse, M. Sawicki, S. G. Ebbinghaus, and G. Schmidt, Yttrium iron garnet thin films with very low damping obtained by recrystallization of amorphous material, Sci. Rep. **6**, 20827 (2016).

[9] H. Chang, P. Li, W. Zhang, T. Liu, A. Hoffmann, L. Deng, and M. Wu, Nanometer-thick yttrium iron garnet films with extremely low damping, IEEE Magn. Lett. **5**, 6700104 (2014).

[10] D. Lachance-Quirion, Y. Tabuchi, A. Gloppe, K. Usami, and Y. Nakamura, Hybrid quantum systems based on magnonics, Appl. Phys. Express **12**, 070101 (2019).

[11] Y. Li, W. Zhang, V. Tyberkevych, W. K. Kwok, A. Hoffmann, and V. Novosad, Hybrid magnonics: Physics, circuits, and applications for coherent information processing, J. Appl. Phys. **128**, 130902 (2020).

[12] A. A. Clerk, K. W. Lehnert, P. Bertet, J. R. Petta, and Y. Nakamura, Hybrid quantum systems with circuit quantum electrodynamics, Nat. Phys. **16**, 257 (2020).

[13] Z. Jiang, J. Lim, Y. Li, W. Pfaff, T. H. Lo, J. Qian, A. Schleife, J. M. Zuo, V. Novosad, and A. Hoffmann, Integrating magnons for quantum information, Appl. Phys. Lett. **123**, 130501 (2023).

[14] Y. Tabuchi, S. Ishino, A. Noguchi, T. Ishikawa, R. Yamazaki, K. Usami, and Y. Nakamura, Coherent coupling between a ferromagnetic magnon and a superconducting qubit, Science **349**, 405 (2015).

[15] D. Lachance-Quirion, S. P. Wolski, Y. Tabuchi, S. Kono, K. Usami, and Y. Nakamura, Entanglement-based single-shot detection of a single magnon with a superconducting qubit, Science **367**, 425 (2020).

[16] S. Rani, X. Cao, A. E. Baptista, A. Hoffmann, and W. Pfaff, High-dynamic-range quantum sensing of magnons and their dynamics using a superconducting qubit, Phys. Rev. Appl. **23**, 064032 (2025).

[17] D. Xu, X. K. Gu, H. K. Li, Y. C. Weng, Y. P. Wang, J. Li, H. Wang, S. Y. Zhu, and J. Q. You, Quantum control of a single magnon in a macroscopic spin system, Phys. Rev. Lett. **130**, 193603 (2023).

[18] Y. Li, T. H. Lo, J. Lim, J. E. Pearson, R. Divan, W. Zhang, U. Welp, W. K. Kwok, A. Hoffmann, and V. Novosad, Unidirectional microwave transduction with chirality selected short-wavelength magnon excitations, Appl. Phys. Lett. **123**, 022406 (2023).

[19] N. Zhu, X. Zhang, X. Han, C.-L. Zou, C. Zhong, C.-H. Wang, L. Jiang, and H. X. Tang, Waveguide cavity opto-magnonics for microwave-to-optics conversion, Optica **7**, 1291 (2020).

[20] C. Liu, S. M. Wu, J. E. Pearson, J. S. Jiang, N. d'Ambrumenil, and A. Bhattacharya, Probing short-range magnetic order in a geometrically frustrated magnet by means of the spin Seebeck effect, Phys. Rev. B **98**, 060415(R) (2018).

[21] R. O. Serha, A. A. Voronov, D. Schmoll, R. Verba, K. O. Levchenko, S. Koraltan, K. Davídková, B. Budinská, Q. Wang, O. V. Dobrovolskiy, M. Urbánek, M. Lindner, T. Reimann, C. Dubs, C. Gonzalez-Ballestero, C. Abert, D. Suess, D. A. Bozhko, S. Knauer, and A. V. Chumak, Magnetic anisotropy and GGG substrate stray field in YIG films down to millikelvin temperatures, npj Spintron. **2**, 29 (2024).

[22] S. Guo, D. Russell, J. Lanier, H. Da, P. C. Hammel, and F. Yang, Strong on-chip microwave photon-magnon coupling using ultralow-damping epitaxial $Y_3Fe_5O_{12}$ films at 2 K, Nano Lett. **23**, 5055 (2023).

[23] G. Li, H. Bai, J. Su, Z. Z. Zhu, Y. Zhang, and J. W. Cai, Tunable perpendicular magnetic anisotropy in epitaxial $Y_3Fe_5O_{12}$ films, APL Mater. **7**, 041104 (2019).

[24] W. Legrand, Y. Kemna, S. Schären, H. Wang, D. Petrosyan, L. Holder, R. Schlitz, M. H. Aguirre, M. Lammel, and P. Gambardella, Lattice-tunable substituted iron garnets for low-temperature magnonics, Adv. Funct. Mater. **36**, 2503644 (2026).

[25] Z. Ye, H. Ling, Y. Ling, and Q. Fu, Critical thickness of yttrium iron garnet thin films with epitaxial interface to get perpendicular magnetic anisotropy, ACS Appl. Electron. Mater. **6**, 2369 (2024).

[26] Y. Meng, P. Chen, W. He, H. Zhuang, J. Li, J. Dong, X. Li, L. Wang, Q. Guo, J. Yang, Y. Ji, X. Shen, X. Yu, G. Yu, J.

Li, X. Han, and R. Yu, A strategy for enhancing perpendicular magnetic anisotropy in yttrium iron garnet films, Small **20**, 2308724 (2024).

[27] J. W. Matthews and A. E. Blakeslee, Defects in epitaxial multilayers: I. Misfit dislocations, J. Cryst. Growth **27**, 118 (1974).

[28] R. People and J. C. Bean, Calculation of critical layer thickness versus lattice mismatch for Ge_xSi_{1-x}/Si strained-layer heterostructures, Appl. Phys. Lett. **47**, 322 (1985).

[29] J. B. Youssef, N. Beaulieu, R. Schlitz, D. Petrosyan, M. Lammel, and W. Legrand, Low-temperature-compatible iron garnet films grown by liquid phase epitaxy, arXiv:2509.06242.

[30] C. Y. Guo, C. H. Wan, M. K. Zhao, H. Wu, C. Fang, Z. R. Yan, J. F. Feng, H. F. Liu, and X. F. Han, Spin-orbit torque switching in perpendicular $Y_3Fe_5O_{12}$/Pt bilayer, Appl. Phys. Lett. **114**, 192409 (2019).

[31] P. Salg, D. Walk, L. Zeinar, A. Radetinac, A. Zintler, R. Jakoby, H. Maune, P. Komissinskiy, and L. Alff, Atomically interface engineered micrometer-thick $SrMoO_3$ oxide electrodes for thin-film $Ba_xSr_{1-x}TiO_3$ ferroelectric varactors tunable at low voltages, APL Mater. **7**, 051107 (2019).

[32] Y. Ruan, P. Schreyer, T. Jiang, F. Liang, A. Arzumanov, M. Dürrschnabel, L. Molina-luna, P. Komissinskiy, and L. Alff, Giant critical thickness in highly conducting epitaxial $SrMoO_3$ electrodes investigated by lift-off membranes, Adv. Funct. Mater. **34**, 2312508 (2024).

[33] R. Dittmann, in *Epitaxial Growth of Complex Metal Oxides*, edited by G. Koster, M. Huijben, and G. Rijnders (Woodhead Publishing, Cambridge, 2015), Chap. 9, pp. 231–261.

[34] T. Suzuki, Y. Nishi, and M. Fujimoto, Defect structure in homoepitaxial non-stoichiometric strontium titanate thin films, Philos. Mag. A **80**, 621 (2000).

[35] Y. Tokuda, S. Kobayashi, T. Ohnishi, T. Mizoguchi, N. Shibata, Y. Ikuhara, and T. Yamamoto, Strontium vacancy clustering in Ti-excess $SrTiO_3$ thin film, Appl. Phys. Lett. **99**, 033110 (2011).

[36] D. J. Keeble, S. Wicklein, L. Jin, C. L. Jia, W. Egger, and R. Dittmann, Nonstoichiometry accommodation in $SrTiO_3$ thin films studied by positron annihilation and electron microscopy, Phys. Rev. B **87**, 195409 (2013).

[37] P. Cao Van, S. Surabhi, V. Dongquoc, R. Kuchi, S. G. Yoon, and J. R. Jeong, Effect of annealing temperature on surface morphology and ultralow ferromagnetic resonance linewidth of yttrium iron garnet thin film grown by rf sputtering, Appl. Surf. Sci. **435**, 377 (2018).

[38] P. Cao Van, H. Kim, T. Nguyen Thi, D. Duong Viet, V. A. Cao, J. Nah, S. J. Park, H. Jin, Y. Jo, S. Y. Park, J. Park, J. M. Yuk, K. J. Kim, and J. R. Jeong, Spin Hall magnetoresistance and the effect of post-annealing temperature in the MOD-grown HoIG, J. Alloys Compd. **941**, 169019 (2023).

[39] Y. Li, W. Cao, V. P. Amin, Z. Zhang, J. Gibbons, J. Sklenar, J. Pearson, P. M. Haney, M. D. Stiles, W. E. Bailey, V. Novosad, A. Hoffmann, and W. Zhang, Coherent spin pumping in a strongly coupled magnon-magnon hybrid system, Phys. Rev. Lett. **124**, 117202 (2020).

[40] J. D. Costa, N. Claessens, G. Talmelli, D. Tierno, F. Amar, T. Devolder, M. Dekkers, F. Ciubotaru, and C. Adelmann, Correlation between structural and magnetic properties of epitaxial YIG films by pulsed laser deposition, ACS Omega **11**, 12612 (2026).

[41] J.-m. Zuo, R. Yuan, Y.-t. Shao, H.-w. Hsiao, S. Pidaparthy, Y. Hu, Q. Yang, and J. Zhang, Data-driven electron microscopy: Electron diffraction imaging of materials structural properties, Microscopy **71**, i116 (2022).

[42] R. Yuan, J. Zhang, and J.-m. Zuo, Lattice strain mapping using circular Hough transform for electron diffraction disk detection, Ultramicroscopy **207**, 112837 (2019).

[43] R. Yuan, J. Zhang, L. He, and J. M. Zuo, Training artificial neural networks for precision orientation and strain mapping using 4D electron diffraction datasets, Ultramicroscopy **231**, 113256 (2021).

[44] J. Fu, M. Hua, X. Wen, M. Xue, S. Ding, M. Wang, P. Yu, S. Liu, J. Han, C. Wang, H. Du, Y. Yang, and J. Yang, Epitaxial growth of $Y_3Fe_5O_{12}$ thin films with perpendicular magnetic anisotropy, Appl. Phys. Lett. **110**, 202403 (2017).

[45] S. J. Tan, W. Zhang, L. Yang, J. Chen, and Z. Wang, Intrinsic defects in yttrium iron garnet: A first-principles study, J. Appl. Phys. **128**, 183904 (2020).

[46] H. Wang, C. Du, P. C. Hammel, and F. Yang, Strain-tunable magnetocrystalline anisotropy in epitaxial $Y_3Fe_5O_{12}$ thin films, Phys. Rev. B **89**, 134404 (2014).

[47] E. I. Ahamed, H. Yamahara, M. S. Sarker, H. Li, K. Morikawa, K. Yamagami, M. Kobayashi, M. Seki, and H. Tabata, Strain-induced reduction of centrosymmetry in rare-earth iron garnet thin films, Adv. Electron. Mater. **11**, 2400735 (2025).

[48] A. Krysztofik, S. Özoğlu, R. D. McMichael, and E. Coy, Effect of strain-induced anisotropy on magnetization dynamics in $Y_3Fe_5O_{12}$ films recrystallized on a lattice-mismatched substrate, Sci. Rep. **11**, 14011 (2021).

[49] A. Vailionis, in *Epitaxial Growth of Complex Metal Oxides*, edited by G. Koster, M. Huijben, and G. Rijnders (Woodhead Publishing, Cambridge, 2015), Chap. 7, pp. 175–207.

[50] N. D. Scarisoreanu, F. Craciun, R. Birjega, V. Ion, V. S. Teodorescu, C. Ghica, R. Negrea, and M. Dinescu, Joining chemical pressure and epitaxial strain to yield Y-doped $BiFeO_3$ thin films with high dielectric response, Sci. Rep. **6**, 25535 (2016).

[51] J. E. Abrão, D. Weltens, R. Mansell, S. van Dijken, and L. Flajšman, Spin-wave propagation at low temperatures in YIG thin films on YSGG substrates, arXiv:2510.04330.

[52] See Supplemental Material at http://link.aps.org/supplemental/10.1103/d3lt-swsx for Supplementary Methods detailing quantitative analysis performed in the manuscript, and Figs. S1–S8, which includes Refs. [24,42,43,53].

[53] J.-M. Zuo and J. C. H. Spence, *Advanced Transmission Electron Microscopy: Imaging and Diffraction in Nanoscience* (Springer, New York, 2017).

[54] Data of electron microscopy and diffraction, magnetic performance, and XRD are available at https://databank.illinois.edu/datasets/IDB-7119850.